MATERIALS SCIENCE

# Room temperature crack-healing in an atomically layered ternary carbide

**Hemant J. Rathod[1], Thierry Ouisse[2], Miladin Radovic[1]*, Ankit Srivastava[1]***



**Ceramic materials provide outstanding chemical and structural stability at high temperatures and in hostile environments but are susceptible to catastrophic fracture that severely limits their applicability. Traditional approaches to partially overcome this limitation rely on activating toughening mechanisms during crack growth to postpone fracture. Here, we demonstrate a more potent toughening mechanism that involves an intriguing possibility of healing the cracks as they form, even at room temperature, in an atomically layered ternary carbide. Crystals of this class of ceramic materials readily fracture along weakly bonded crystallographic planes. However, the onset of an abstruse mode of deformation, referred to as kinking in these materials, induces large crystallographic rotations and plastic deformation that physically heal the cracks. This implies that the toughness of numerous other layered ceramic materials, whose broader applications have been limited by their susceptibility to catastrophic fracture, can also be enhanced by microstructural engineering to promote kinking and crack-healing.**

## INTRODUCTION

The lack of materials capable of withstanding extreme environments, more often than not, imposes the greatest technological barrier to the development and deployment of a host of next-generation technologies, such as efficient jet engines, hypersonic flights, and safer nuclear reactors (*1*–*4*). While ceramic materials provide outstanding chemical and structural stability at high temperatures and in hostile environments, their insufficient plastic deformability and damage tolerance compared to metallic materials severely limit their applicability (*5*, *6*). In particular, at room temperature, ceramic materials readily undergo catastrophic fracture by cohesive bond breaking at the crack tip. Traditional approaches to partially overcome this issue in ceramic materials rely on microstructure-specific toughening mechanisms such as crack-deflection, crack-bridging, microcracking, and stress-induced phase transformations (*5*, *6*). The quest to enhance damage tolerance also includes the development of nature-inspired ceramic-based (hybrid) materials with hierarchical structures that can trigger a combination of toughening mechanisms (*7*–*12*). Although activating toughening mechanisms during crack growth can postpone catastrophic fracture, a more potent toughening mechanism is to heal the cracks as they form.

Crack-healing requires local flow of material to close and heal the cracks by physical or chemical interactions (*13*). In principle, this can be realized intrinsically (without healing agents) or extrinsically (with healing agents) and autonomously (without external triggers) or nonautonomously (with external triggers) and is not limited to a single class of materials (*13*). Nonetheless, polymers and polymer composites (*14*–*16*), as well as cementitious materials (*17*, *18*), are by far the biggest beneficiaries of crack-healing mechanisms, while only limited successes have been reported for ceramic (*19*–*23*) and metallic (*24*) materials. In ceramic materials, except for a few, crack-healing has been mainly realized extrinsically by incorporating healing agents and/or nonautonomously (postmortem) by applying high pressure at high temperatures. In very few cases, autonomous crack-healing in ceramic materials is achieved by high-temperature oxidation of the cracks that form during loading (*20*–*23*). Crack-healing by high-temperature oxidation, however, has several limitations. For example, it at least requires the presence of an oxidative phase, accessibility of the crack surfaces to the oxidizing environment, and good adhesion of the oxide scale to the crack surfaces. Also, selective oxidation of some microstructural features (e.g., grain boundaries) can lead to stress concentration sites, while thermal expansion mismatch between the material and the crack-healing oxide can lead to crack initiation during thermal cycling.

Here, we demonstrate that intrinsic and autonomous crack-healing is possible even at room temperature in crystalline atomically layered ceramic materials such as MAX phases (*25*–*27*) by kinking-induced crystallographic rotation and plastic deformation. MAX phases are a family of ternary carbides/nitrides with general formula $M_{n+1}AX_n$, where M is an early transitional metal, A is mostly an element from groups 13 to 16, X is carbon or nitrogen, and $n$ varies from 1 to 3, and comprise alternating $M_{n+1}X_n$ and A atomic layers within a hexagonal crystal structure (*25*–*27*). Numerous studies have shown that several individual grains in polycrystalline MAX phases can readily kink under a variety of external loading conditions, such as tensile, compressive, creep, fatigue, and impact (*28*–*33*). Kinking leads to localized plastic deformation in bands referred to as "kink-bands," wherein the material is microstructurally or crystallographically misoriented from the unkinked region. Kinking is not unique to MAX phases and has been observed in a variety of natural (*34*–*37*) and engineered (*38*–*46*) materials. While in engineering composites kinking results in failure (*40*–*42*), in polycrystalline MAX phases it has been postulated that kinking restricts the rapid crack growth along the weakly bonded planes by crack-bridging (*28*, *29*) and is solely responsible for their unconventional damage tolerance (*25*, *26*, *30*). However, our discovery that kinking in MAX phases heals the cracks as they form reveals that it is an even more potent toughening mechanism than previously envisaged.

Specifically, we report on the evolution of kinking and its role in crack-healing during room temperature in situ indentation of carefully grown single crystals of the $Cr_2AlC$ MAX phase (fig. S1) (*47*) in a scanning electron microscope (SEM). The in situ indentation is carried out using an in-house design and build fixture that allows us

[1]Department of Materials Science and Engineering, Texas A&M University, College Station, TX 77843, USA. [2]Université Grenoble Alpes, CNRS, Grenoble INP, LMGP, F-38000 Grenoble, France.
*Corresponding author. Email: mradovic@tamu.edu (M.R.); ankit.sri@tamu.edu (A.S.)

to load single-crystal specimens with a punch along predetermined directions, with and without lateral deformation constraint. The lateral deformation constraint considered here mimics the presence of neighboring grains that affect the deformation and damage evolution in individual grains of a polycrystalline aggregate. Until we used this fixture, it was extremely difficult to study the effect of local deformation constraint on kinking and the implications of kinking on toughening in MAX phases from mechanical testing of their polycrystalline aggregates (*25*, *26*, *28*–*32*) or micropillars milled from individual grains (*48*–*50*).

## RESULTS

### In situ indentation of freestanding single crystals

We first carried out in situ indentation experiments on freestanding single-crystal specimens of $Cr_2AlC$ (Fig. 1A). The free-standing crystals were indented along the $\langle 11\bar{2}0\rangle$ crystallographic direction, and the indentation force-depth response (Fig. 1B) was recorded together with secondary electron (SE)–SEM images of the specimen surface (Fig. 1, C to E). It is well established by now that the basal slip systems, $\{0001\}\langle 11\bar{2}0\rangle$, are the only active slip systems for crystallographic slip in MAX phases at room temperature (*25*). Thus, loading a crystal of MAX phase along the $\langle 11\bar{2}0\rangle$ crystallographic direction leads to zero resolved shear stress on the basal slip systems, and no plastic deformation due to slip is expected under these circumstances. On the other hand, compressing the crystal along the $\langle 11\bar{2}0\rangle$ crystallographic direction leads to Poisson expansion of the crystal along $\langle 01\bar{1}0\rangle$ and $\langle 0001\rangle$ (normal to the basal plane) crystallographic directions. The expansion of the MAX phase crystal, in particular, normal to the basal planes facilitates initiation of cleavage cracks between the weakly bonded A and $M_{n+1}X_n$ layers (*25*). With progressive indentation, some of these cracks propagate rapidly through the entire specimen (Fig. 1, D and E). Note that the expansion of the material underneath the indenter in these experiments is limited because the specimen surface in direct contact with the indenter undergoes slight frictional adhesion. As a result, the cracks that form directly under the indenter do not grow rapidly, and the ligaments between these cracks buckle and rotate (Fig. 1F). The buckling and rotation of the ligaments, in turn, arrests the growth of the cracks during loading. However, upon unloading, these buckled ligaments snap back to their original configuration, and the specimen fractures only in few pieces (Fig. 1G). Additional postmortem observation of the fractured pieces of the specimen using polarized light shows no color contrast, suggesting a lack of local changes in the crystallographic orientation of the initial single-crystal specimen.

### In situ indentation of constrained single crystals

Next, we carried out in situ indentation experiments on single-crystal specimens of $Cr_2AlC$ that were placed in our in-house fixture and subjected to a deformation constraint along the $\langle 0001\rangle$ crystallographic directions, i.e., normal to the basal planes (Fig. 2A). To ensure that the deformation constraint imposed by the fixture is not entirely rigid, a thin layer of epoxy was introduced between the specimen and the fixture. Note that before the onset of indentation, the specimen inside the fixture is stress free. Here as well, the specimens were indented along the $\langle 11\bar{2}0\rangle$ crystallographic direction and the indentation response (Fig. 2B) was recorded together with the SE-SEM images of the specimen surface (Fig. 2, C to H).

As in the case of the unconstrained indentation, here as well, first multiple cleavage cracks initiate along the basal planes in the



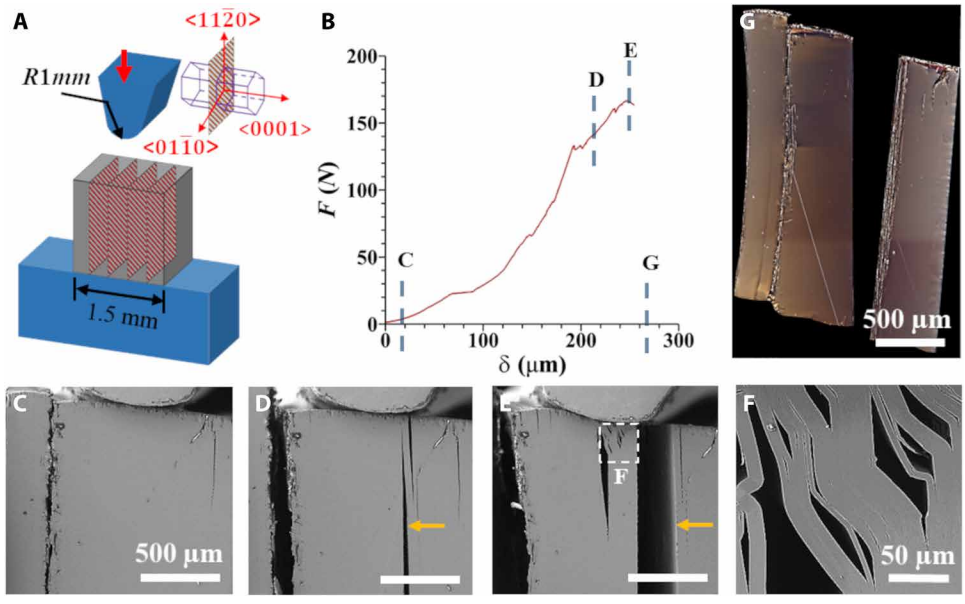


**Fig. 1. In situ indentation of a freestanding single-crystal specimen of $Cr_2AlC$.** (**A**) Schematic of the experimental setup in which a freestanding single-crystal specimen of $Cr_2AlC$ is indented along the $\langle 11\bar{2}0\rangle$ crystallographic direction using a punch with a cylindrical tip. (**B**) Indentation force (*F*)–depth (δ) response. (**C** to **E**) SEM images showing the initiation and propagation of cleavage cracks along the basal planes, i.e., {0001} planes, and buckling of the ligaments between the cracks underneath the indenter. A dominant cleavage crack is marked with an arrow in (D) and (E). (**F**) High-magnification SEM image of the region marked with a dashed box labeled F in (E) showing buckling and rotation of the ligaments between the cleavage cracks. (**G**) Post-deformation polarized light optical microscopy image showing cleavage of the entire specimen parallel to the indentation direction and the absence of any local changes in the crystallographic orientation. The scale bars in (C) to (E) are the same. The indentation depth corresponding to SEM images in (C) to (E) is marked in (B).

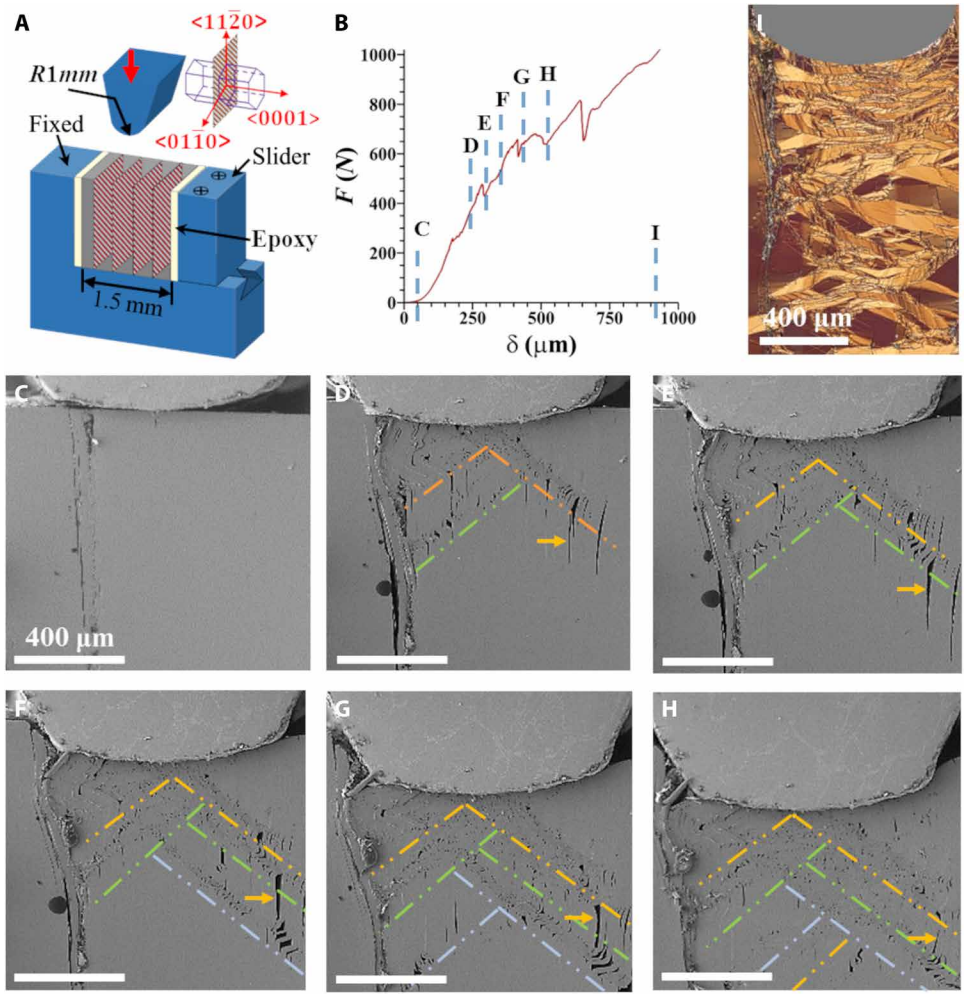


**Fig. 2. In situ indentation of a constrained single-crystal specimen of $Cr_2AlC$.** (**A**) Schematic of the experimental setup in which a single-crystal specimen of $Cr_2AlC$ is indented along the ⟨11$\bar{2}$0⟩ crystallographic direction using a punch with a cylindrical tip while being constrained along the ⟨0001⟩ direction, i.e., normal to the basal planes. (**B**) Indentation force (*F*)–depth (δ) response. (**C** to **H**) SEM images showing progressive initiation of cleavage cracks, kinking of the ligaments between the cracks, and localized plastic deformation in bands (traced with dashed double dotted lines) that are inclined to the indentation axis. An arrow follows the growth, opening, and finally healing of one of the basal plane cleavage cracks in (D) to (H). (**I**) Post-deformation polarized light optical microscopy image showing irreversible polycrystallization of the initial single-crystal specimen. The scale bars in (C) to (H) are the same. The indentation depth corresponding to SEM images in (C) to (H) is marked in (B).

specimens during loading (Fig. 2 and fig. S2). However, because of the deformation constraint normal to the basal planes, in this case, the cracks do not propagate rapidly through the entire specimen. Furthermore, and somewhat surprisingly, despite increase in load, the cracks are seemingly arrested by the onset of plastic deformation in bands inclined to the indentation axis (indicated by the broken lines in Fig. 2, D and E) and with continued loading, more cracks and plastic deformation bands (Fig. 2, F to H) appear in the specimens. Even more surprisingly, the cleavage cracks that previously initiated, instead of propagating along the basal planes, tend to slightly open in a direction normal to the basal plane before beginning to close (an arrow follows one such crack in Fig. 2, D to H). This chain of events continues with the progressive loading, and unlike in the case of unconstrained specimens (Fig. 1), it allows the indentation of the specimen to continue to a greater depth with increasing force (Fig. 2B), without the specimen being fractured into pieces (Fig. 2I). Moreover, after complete unloading, the post-deformation optical images of $Cr_2AlC$ single-crystal specimens under polarized light show extensive color contrast throughout the deformed specimen, suggesting notable permanent changes in the local crystallographic orientation that resembles a polycrystalline microstructure (Fig. 2I and fig. S3). The apparent polycrystallization (Figs. 3 and 4) occurs because the localized plastic deformation bands that form in the constrained single-crystal specimens are actually kink-bands that cause progressive crystallographic reorientation of the material (Fig. 5). The grain structure in the polycrystallized specimens also varies through the depth of the specimen. As shown in Fig. 2I (and in fig. S3), underneath the indenter, the grains are relatively thinner and the grain boundaries are almost normal to the indentation axis as compared to the regions far away from the indent, where the grains are thicker, and the grain boundaries are inclined at relatively larger angles to the indentation axis.

## Polycrystallization and crack-healing

Careful postmortem examination of the deformed specimens upon complete unloading and its removal from the fixture revealed the

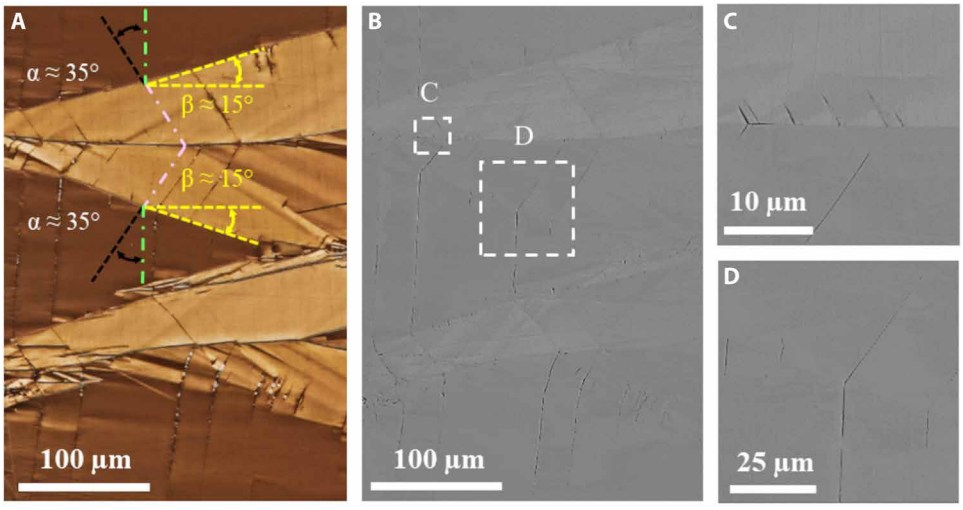


**Fig. 3. Polycrystallization and crack healing in a constrained single-crystal specimen of $Cr_2AlC$ after in situ indentation.** (**A**) Post-deformation high-magnification polarized light optical microscopy image showing kinking-induced irreversible polycrystallization of the initial single-crystal specimen at a location (roughly 600 μm) below the remnant impression of the indenter. The average in-plane rotation (α) of the material in select kink-bands together with the inclination (β) of the boundaries of these kink-bands is also marked in (A). (**B**) SEM image of the same region in (A) showing physically healed cracks inside the kink-bands. (**C** and **D**) Even higher-magnification SEM images of the regions are marked with dashed boxes labeled C and D in (B), respectively, showing healed cracks inside the kink-bands and the absence of cracks along the kink-band boundaries.

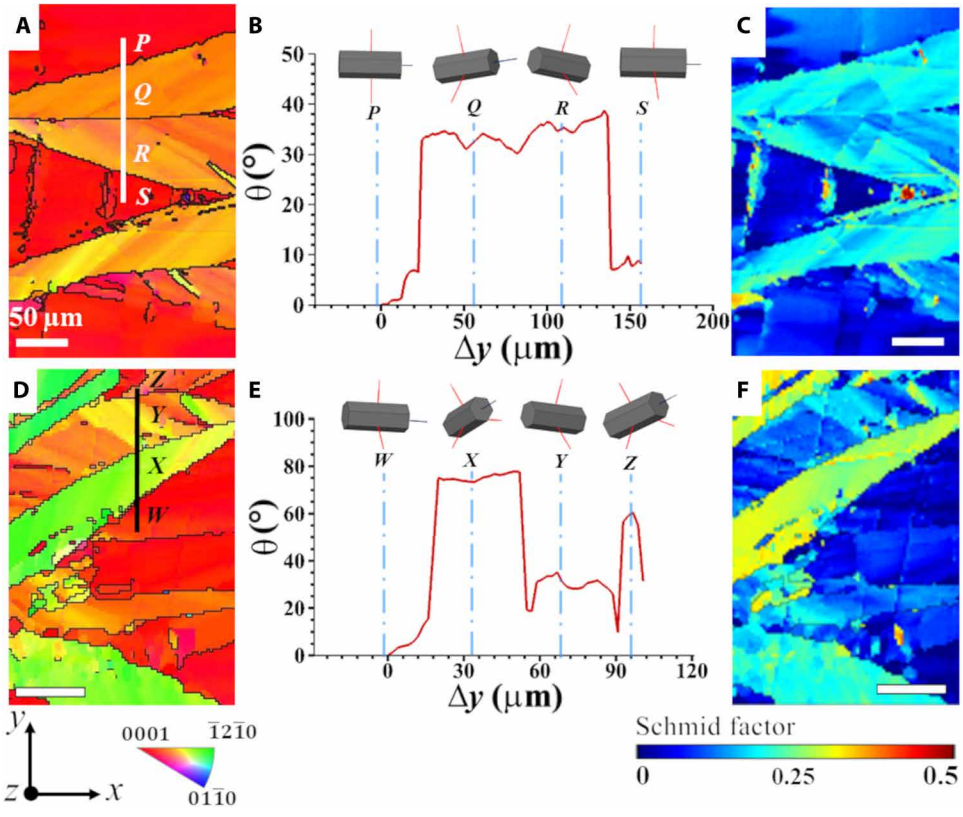


**Fig. 4. Kinking-induced crystal reorientation in a constrained single-crystal specimen of $Cr_2AlC$ after in situ indentation.** (**A**) EBSD *x*-IPF map quantifying the local crystal orientation in the kink-bands shown in Fig. 3A. (**B**) Crystal misorientation angle (θ) along the *P-S* line in (A) together with the local orientation of the hexagonal unit cell at four locations. (**C**) Contour plot of the classical maximum Schmid factor for the basal slip systems with loading axis along the $\langle 11\bar{2}0\rangle$ crystallographic direction in the region shown in (A). (**D**) EBSD *x*-IPF map of a relatively more deformed region. (**E**) Crystal misorientation angle (θ) along the *W-Z* line in (D) together with the local orientation of the hexagonal unit cell at four locations. (**F**) Contour plot of the classical maximum Schmid factor for the basal slip systems with loading axis along the $\langle 11\bar{2}0\rangle$ crystallographic direction in the region shown in (D). Note that $\langle 11\bar{2}0\rangle$ and $\langle 0001\rangle$ crystallographic orientations of the initial single-crystal specimen were along *y* and *x* axes, respectively. The scale bars in (A), (C), (D), and (F) are the same.

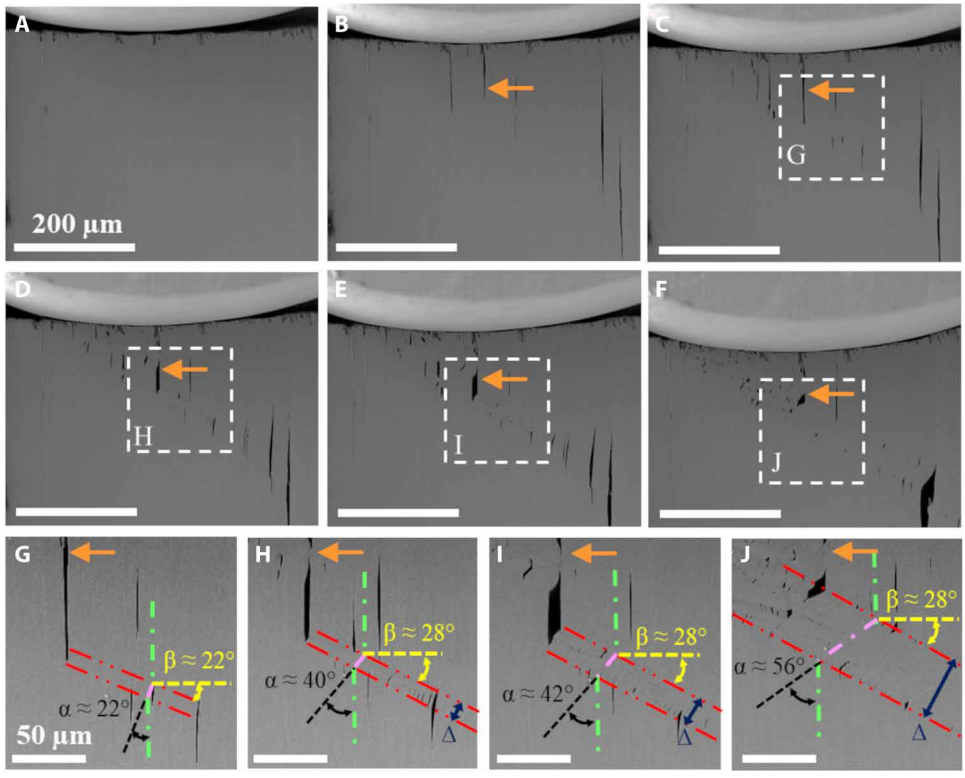


**Fig. 5. Evolution of cracking, kinking, and crack-healing during in situ indentation of a constrained single-crystal specimen of $Cr_2AlC$.** A series of SEM images showing the sequence of events at a fixed location during progressive indentation. (**A**) Specimen surface at the beginning of indentation. (**B**) Initiation of multiple parallel cleavage cracks along the basal planes. (**C**) Growth and opening of the cracks. (**D**) Buckling and kinking of the ligaments between the basal plane cracks, formation of kink-band, and crack growth arrest. (**E** and **F**) Growth and widening of the kink-band and crack-healing. (**G** to **J**) High-magnification SEM images of the regions marked with dashed boxes labeled G to J in (C) to (F), respectively, showing the sequence of events leading to crack-healing: First, a thin kink-band initiates; next, with increasing deformation, the material in the kink-band rotates, while the kink-band grows and widens; and finally, heals the cracks. In (B) to (J), an arrow follows the growth, opening, rotation, and, finally, healing of one of the basal plane cracks. The boundaries of one of the kink-band in (G) to (J) are traced by dashed double dotted (red) lines, and the average in-plane rotation (α) of the material in the kink-band, together with the inclination (β) of the kink-band boundaries, is also marked. The scale bars in (A) to (F) and (G) to (J) are the same.

absence of any large cracks (Fig. 3). Even at high resolution (Fig. 3, C and D, and fig. S3), we do not see any large cracks inside the kinking-induced misoriented regions or along the kink-band (i.e., misorientation) boundaries. This is remarkable, because any compressive stress that builds up normal to the basal planes during loading due to the deformation constraint imposed by the fixture is relieved once the specimen is removed from the fixture. This suggests that the crack closure is not elastic, but the cracks are physically healed during loading; otherwise, relaxation of the compressive stress that built up normal to the basal planes would have caused further crack opening upon unloading. Note that the occasional inclined hairline-like features inside the kink-bands in Fig. 3 (A and B) are likely surface marks from physically healed cracks.

The local crystal orientation in the kink-bands was examined using electron backscatter diffraction (EBSD) in an SEM. The EBSD inverse-pole figure (IPF) maps of the kink-bands show that the material in the kink-bands within initially single-crystal $Cr_2AlC$ specimens undergoes not only in-plane (in the *x*-*y* plane) but also out-of-plane (in the *x*-*z* and *y*-*z* planes) rotations, as shown in Fig. 4 and fig. S4. That is, the crystal rotation in the kink-bands leads to not only tilting but also twisting of the basal planes. This is in direct contrast with kinking in layered composite materials, where the material in the kink-bands predominantly undergoes in-plane rotation (*41*). Also, the extent of the material rotation in the kink-bands in $Cr_2AlC$ varies markedly through the specimen. For instance, in the region shown in Fig. 3A, the material in the two kink-bands that morphologically resemble corners of an eye has undergone an average rotation (θ) of approximately 35° in opposite directions, compared to the initial orientation of the specimen (Fig. 4, A and B), while in relatively more deformed regions the average rotation of the material in (rather thin) kink-bands can be greater than 75° (Fig. 4, D and E). The rotation of the material in the kink-bands is such that it increases the Schmid factor for the basal slip system that, in turn, increases the resolved shear stress required to initiate plastic deformation by crystallographic slip in the rotated regions (Fig. 4, C and F). Note that the inclination (α) of the occasional hairline-like residual markings of the physically healed cracks (Fig. 3A) is roughly the same as the misorientation angle (θ) of the material in the kink-bands (Fig. 4, A and B).

## Kinking as a crack-healing mechanism

The chain of events involving cracking, kinking, and crack-healing with increasing indentation load under deformation constraint normal to basal planes was repetitively observed in multiple

specimens (Figs. 2 and 5 and figs. S2 and S5). In all of these specimens, with progressive indentation, first multiple parallel cracks initiate and grow along the basal planes. Next, the ligaments between these parallel cracks buckle and kink, arresting the further crack growth, while the kinking-induced local crystallographic rotation of the material in the ligament at least initially increases the driving force for plastic deformation by crystallographic slip in the kink-bands. The evolution of the in-plane shear strain, $\gamma_{xy}$, in the kink-bands (while neglecting out-of-plane rotations and assuming basal planes to be inextensible and incompressible) can be approximated as (*51*)

$$\gamma_{xy} = \tan(\beta) - \tan(\beta - \alpha) \quad (1)$$

where α is the in-plane rotation of the crystal inside the kink-bands and β is the inclination of the kink-band boundaries (as described in Fig. 3A). The evolution of α during in situ indentation experiments can be simply determined by following the rotation of the basal plane cracks within the kink-bands, while any change in the inclination of the kink-band boundaries, β, can be directly monitored (Fig. 5). Quantifying the evolution of α and β with increasing loading during in situ SEM experiments shows that both the in-plane rotation of the crystal in the kink-bands and (to an extent and at least initially) the inclination of the kink-band boundaries increase with progressive loading. The increase in the values of α and β with progressive loading is such that the shear strain in the kink-bands continues to increase, for example, from Fig. 5G the value of $\gamma_{xy} \approx 0.4$, while at higher load in Fig. 5J the value of $\gamma_{xy} \approx 1$. This shows that, unlike deformation twinning, crystallographic rotation of the material, as well as the associated shear deformation during kinking, is not crystallographically restricted, but it continues to evolve within kink-bands with progressive loading.

However, although the shear strain in the kink-bands is continuously increasing and the growth of the cracks along the basal planes is arrested, the portion of the cracks within the kink-bands does first partially open before beginning to close (Fig. 5, G to J). An approximate analysis of the kink-band geometry, again, by neglecting out-of-plane rotations and assuming basal planes to be inextensible and incompressible shows that the nominal volumetric strain, $\Delta V/V$, in the kink-band follows (*51*)

$$\frac{\Delta V}{V} = \cos(\beta - \alpha)\sec(\beta) - 1 \quad (2)$$

Thus, as the material inside the kink-band starts to rotate and the plastic deformation evolves, the material volume first tends to dilate before it begins to contract as α approaches (Fig. 5J) or exceeds 2β (fig. S6). The rotation of the material in the kink-bands, together with the associated contraction of the material volume, leads to permanent tilting, twisting, and closure of the portion of the basal plane cracks that lie within the kink-bands. Finally, the growth and widening of multiple adjacent kink-bands lead to permanent distortion and closure or simply physical healing of the entire length of the basal plane cracks (Fig. 5 and fig. S2). This explains why the cracks do not open upon unloading, i.e., relaxation of any compressive stresses that built up normal to the basal planes during loading. Also, note that the initial dilation of the material in the kink-bands not only causes the existing cracks to open but also can initiate secondary cracking within the kink-bands (fig. S5). Nevertheless, all these cracks start to heal once $\alpha \rightarrow 2\beta$.

### Kink-boundary rotation and secondary kinking

Interestingly enough, continued indentation of the constrained specimens to sufficiently higher load levels results in the rotation of the kink-band boundaries away from the indentation axis so that their angle of inclination, β, now starts to decrease (fig. S7). Furthermore, continued loading of the specimens to sufficiently higher load levels also triggers secondary kinking (figs. S2 and S6). These secondary kink-bands mostly initiate from the primary kink-band boundaries or from the partially healed cracks. These observations can be rationalized based on our recent findings that the crystallographic slip in MAX phases does not follow classical Schmid law, and in this material system, slip depends not only on the resolved shear stress but also on the stress normal to the slip planes (*50*). Thus, the crystallographic rotation of the material in the kink-bands, in particular that of the basal planes, first increases the resolved shear stress (driving force for slip), but with continued rotation, the compressive stress normal to the basal planes that resists further slip also increases. The decrease in the extent of plastic deformation due to increased resistance to slip past sufficient rotation of the material in the kink-bands is then compensated by the activation of deformation mechanisms such as the rotation of the kink-band boundaries and secondary kinking. The rotation of the kink-band boundaries and the formation of secondary kink-bands at higher load levels also rationalize the observed variation in the grain structure through the depth in the deformed specimens (fig. S3).

### In situ uniaxial compression of as-grown single crystals and kinking-healed specimens

The results presented thus far show that the onset of kinking during the indentation of constrained single crystals of $Cr_2AlC$ at room temperature leads to physical healing of the cracks as they form. Nevertheless, a question arises as to what extent the strength of the material is restored by kinking-induced crack-healing. To answer this question, we carried out in situ uniaxial compression tests on (freestanding) as-grown single crystals and kinking-healed specimens. Both the as-grown single crystals and kinking-healed specimens were compressed along the same direction as in the indentation experiments, and the force-displacement response was recorded together with SE-SEM images of the specimen surface.

A comparison of the engineering compressive stress-strain (normalized force-displacement) response of the as-grown single crystals and kinking-healed specimens shows that the kinking-healed specimens exhibit significantly higher compressive strength than the as-grown single crystals (Fig. 6). The as-grown single crystals undergo cleavage cracking along the weak basal planes at a very early stage of deformation (fig. S8). While some of these early-stage cracks that form directly under the punch do not grow rapidly due to slight frictional adhesion between the specimen surface and the punch, with progressive deformation, more cracks initiate and several of them, which fracture the specimen into pieces, propagate rapidly. On the contrary, in the kinking-healed specimens, cleavage cracks initiate at higher load levels at locations with relatively large pockets of unkinked regions (fig. S9). Moreover, the cracks in the kinking-healed specimens do not propagate rapidly through the specimen, resulting in a rather graceful failure without the specimen fracturing into pieces.

We also analyzed the reopening resistance of several physically healed cracks in the kinking-healed specimens during in situ uniaxial compression tests (Fig. 7 and fig. S10). To this end, we first

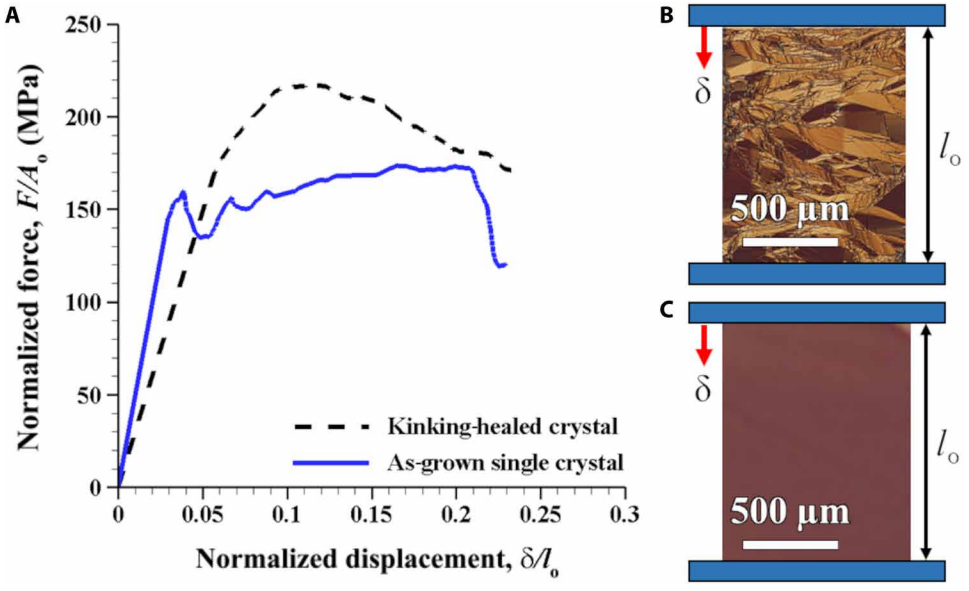


**Fig. 6. Comparing the engineering compressive stress-strain response of an as-grown single-crystal and kinking-healed specimen of $Cr_2AlC$.** The kinking-healed specimen considered here is taken from the single-crystal specimen that was subjected to in situ indentation under deformation constraint normal to the basal planes, as shown in Fig. 2. (**A**) Comparison of the engineering stress-strain [normalized force ($F/A_0$)–displacement ($\delta/l_0$), where $A_0$ and $l_0$ are the initial cross-sectional area and length of the specimen, respectively] response of an as-grown single-crystal and kinking-healed specimen showing improved mechanical performance of the kinking-healed specimen. (**B** and **C**) Schematic of the experimental setup in which the kinking-healed and as-grown single-crystal specimens are subjected to uniaxial compression together with the polarized light optical microscopy images showing the kinking-induced polycrystallized and initial single-crystal microstructures of the respective specimens.

identified several cracks that are physically healed (i.e., underwent permanent tilting, twisting, and closure) by the onset of kinking during in situ indentation experiments under deformation constraint normal to the basal planes (Fig. 7, A to D). These same cracks are then tracked during in situ uniaxial compression tests (Fig. 7, E to H). Our results show that the physically healed cracks (even with length greater than hundreds of micrometers) do not easily reopen up to imposed load levels comparable to the compressive strength of the kinking-healed material. This is noteworthy because the compressive strength of the kinking-healed material is significantly higher than that of the as-grown single crystals.

## DISCUSSION

In summary, it is evident from our results that catastrophic fracture of atomically layered ceramic materials, such as $Cr_2AlC$, can be effectively overcome by not only suppressing the crack growth along the weakly bonded planes but also healing them as they form. For instance, by indenting unconstrained specimens, we showed that even a small Poisson's expansion of the crystal normal to the weakly bonded basal planes is enough to cause initiation and rapid growth of cracks along these planes. However, indentation of these materials while under slight deformation constraint normal to the weakly bonded basal planes enables buckling and kinking of the ligaments between multiple parallel cracks, and formation of kink-bands. Once a kink-band forms, the faces of the portion of the crack that lie within the kink-band undergo permanent tilting, twisting, and closure, leading to physical healing. Furthermore, the growth and widening of multiple adjacent kink-bands lead to physical healing of the entire crack with length greater than hundreds of micrometers.

The importance of this finding cannot be overstated as this explains the puzzling observation that the MAX phases, instead of undergoing catastrophic fracture, demonstrate unconventional damage tolerance (*25*, *26*). The unconventional damage tolerance of polycrystalline MAX phases not only is limited to monotonic compressive loading but also has been observed under a variety of loading conditions (*28*–*32*). From our results, it can be concluded that, in polycrystalline MAX phase aggregates, even the grains that are oriented for easy cleavage along weakly bonded planes can undergo kinking due to the deformation constraint imposed by the neighboring grains and consequently heal the cracks. Thus, the kinking-induced crack-healing mechanism endows these otherwise brittle materials with exceptional resistance to catastrophic fracture. This also implies that the toughness of this class of atomically layered ceramic materials can be further enhanced by carefully designing microstructures to promote extensive kinking and crack-healing.

In ceramic materials, limited autonomous crack-healing, i.e., healing of the cracks as they form during loading, has been previously realized by high-temperature oxidation of the cracks (*21*–*23*). However, we are not aware of any realization of intrinsic and autonomous crack-healing at room temperature in a monolithic ceramic material. Although we have demonstrated room temperature kinking-induced crack-healing in a particular class of atomically layered ceramic material, i.e., MAX phases, it should be noted that MAX phases are an extremely diverse class of material with approximately 155 MAX phase compositions found to date (*27*). Moreover, kinking is not unique to MAX phases and has also been observed in a variety of other atomically layered ceramic materials, and thus, it is reasonable to assume that kinking-induced crack-healing can be achieved in these materials as well. These other atomically layered ceramic materials include graphite (*37*), micas (*34*), hexagonal

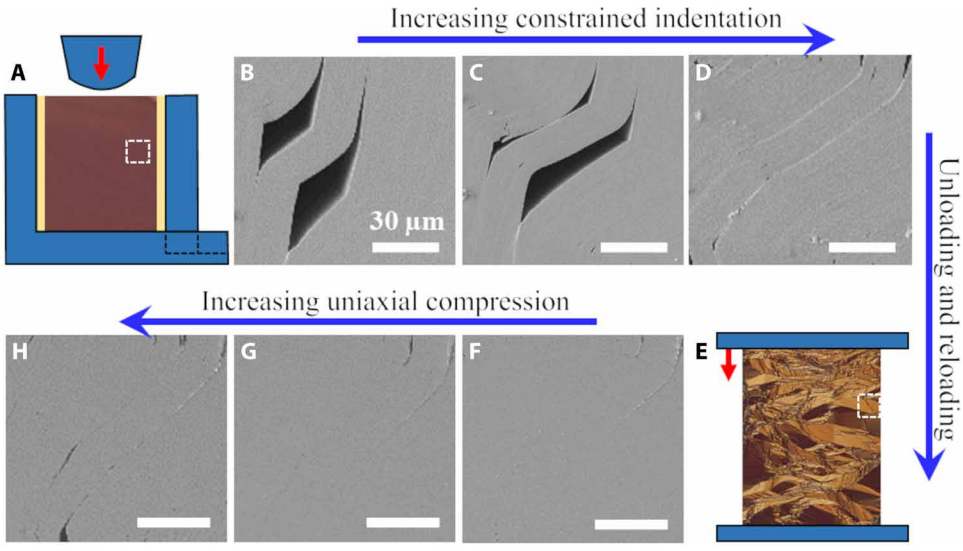


**Fig. 7. Kinking-induced crack-healing in a constrained single-crystal specimen of $Cr_2AlC$ during in situ indentation and reopening resistance of the same healed cracks during in situ uniaxial compression.** (**A**) Schematic of the experimental setup in which an as-grown single-crystal specimen is subjected to indentation under deformation constraint normal to the basal planes. (**B** to **D**) SEM images showing kinking-induced crack-healing with increasing constrained indentation. (**E**) Schematic of the experimental setup in which the kinking-healed specimen is subjected to uniaxial compression. (**F** to **H**) SEM images of the same region in (B) to (D) showing negligible opening of the healed cracks during uniaxial compression. The scale bars in (B) to (D) and (F) to (H) are the same.

carbides (*43*), boron nitride (*44*), and layered borides (*46*), among others, whose broader applications have been limited by their poor damage tolerance and propensity to cleave along weakly bonded planes.

## MATERIALS AND METHODS

### Material synthesis

Single crystals of the $Cr_2AlC$ MAX phase were synthesized using a flux growth method in an induction-heated $Al_2O_3$ crucible based, in part, on a previous work (*47*). Flux composition (in atomic fraction) was $X_{Cr} = 0.354$, $X_{Al} = 0.566$, and $X_C = 0.08$. Carbon was introduced at 1650°C by dipping a rotating graphite rod into the flux. This allowed precise control of the carbon content and prevented the formation of unwanted $Al_4C_3$ and subsequent breaking of the crucible during temperature ramping. After 30 min, the temperature was decreased to 1600°C in 20 min. Next, nucleation and crystal growth were achieved by slow cooling to 1100°C over 5 days. Last, the single crystals were extracted from the solidified flux by HCl etching.

### Sample preparation for in situ indentation testing

As-grown single crystals of $Cr_2AlC$ were first coated with epoxy to avoid fracture in the single crystal by cleavage cracking along the weakly bonded Al and $Cr_2C$ planes during machining and polishing. The epoxy-coated as-grown single crystals were carefully machined into small cuboids of dimensions 2 mm × 2 mm × 1.5 mm using a diamond wire saw. Next, the four faces of the cuboids that are normal to the basal planes (i.e., the $\langle 01\bar{1}0\rangle$ and $\langle 11\bar{2}0\rangle$ faces) of the crystal were mechanically polished up to 0.1-μm diamond suspension and fine-polished with 0.05-μm colloidal silica. The final cuboidal shaped specimens also contained thin (~150-μm-thick) layers of epoxy on the faces of the cuboids that are parallel to the basal planes of the crystal.

### In situ indentation tests

The in situ indentation tests were carried out inside a Tescan FERA-3 SEM using a miniature tension-compression module by Kammrath & Weiss and an in-house design and build fixture. The in-house in situ indentation fixture was machined from a solid block of A2 (air-hardened, 60 RC) tool steel. As shown in Fig. 2A, the fixture comprises a fixed wall and a sliding wall equipped with two tightening screws. The cuboidal specimen is first placed between the fixed and the sliding wall, with the basal planes being parallel to the walls, and then the sliding wall is moved toward the specimen and fixed using the tightening screws. Although the specimen is confined between the two walls, before the onset of any deformation, the specimen inside the fixture is stress free. Note that for the unconstrained tests (Fig. 1A), the specimen is not confined between the walls. Next, a punch with a cylindrical tip of 1-mm radius also machined from A2 (air-hardened, 60 RC) tool steel is used to indent the specimen along a direction parallel to the basal planes at a crosshead speed of 0.5 μm/s. During the indentation, the indentation force-depth response was continuously recorded, while the test was interrupted at regular indentation depth to capture the SE-SEM images of one of the specimen surfaces.

### Sample preparation for in situ uniaxial compression testing

As-grown single-crystal and kinking-healed specimens (i.e., single-crystal specimens that were subjected to in situ indentation under deformation constraint normal to the basal planes; Fig. 2) of $Cr_2AlC$ were carefully machined into small cuboids of dimensions 1 mm × 1.2 mm × 1.5 mm using a diamond wire saw. Next, all the faces (except the two faces parallel to the basal planes of the initial single crystal) of the cuboids were mechanically polished up to 0.1-μm diamond suspension and fine-polished with 0.05-μm colloidal silica.

### In situ uniaxial compression tests

The in situ uniaxial compression tests were carried out inside a Tescan FERA-3 SEM using a miniature tension-compression module by Kammrath & Weiss and a simple compression test fixture. The compression test fixture consists of two tungsten carbide plates, between which the cuboidal specimens were subjected to uniaxial compression at a crosshead speed of 0.5 μm/s, as shown schematically in Fig. 6 (B and C). During the uniaxial compression, the force-displacement response was continuously recorded, while the test was interrupted at regular displacements to capture the SE-SEM images of one of the specimen surfaces.

### Microstructural characterization

The microstructural characterization of the as-grown and deformed single-crystal specimens of $Cr_2AlC$ was carried out by SE-SEM imaging, EBSD, and polarized light optical microscopy. The SE-SEM imaging and EBSD were carried out using a Tescan FERA-3 SEM equipped with a NordlysNano EBSD detector by Oxford Instruments, and optical microscopy was carried out using an Olympus DSX500 digital microscope equipped with polarized light and live panorama options. The EBSD scan was carried out at an operating voltage of 10 kV and with a step size of 2 μm. The EBSD pattern was indexed using the $Cr_2AlC$ phase, and postprocessing was carried out using HKL Channel 5 software by Oxford Instruments.

## SUPPLEMENTARY MATERIALS

Supplementary material for this article is available at http://advances.sciencemag.org/cgi/content/full/7/33/eabg2549/DC1

## REFERENCES AND NOTES


1. J. J. Bertin, R. M. Cummings, Fifty years of hypersonics: Where we've been, where we're going. *Prog. Aerosp. Sci.* **39**, 511–536 (2003).
2. J. H. Perepezko, The hotter the engine, the better. *Science* **326**, 1068–1069 (2009).
3. N. P. Padture, Advanced structural ceramics in aerospace propulsion. *Nat. Mater.* **15**, 804–809 (2016).
4. J. Knaster, A. Moeslang, T. Muroga, Materials research for fusion. *Nat. Phys.* **12**, 424–434 (2016).
5. M. E. Launey, R. O. Ritchie, On the fracture toughness of advanced materials. *Adv. Mater.* **21**, 2103–2110 (2009).
6. R. O. Ritchie, The conflicts between strength and toughness. *Nat. Mater.* **10**, 817–822 (2011).
7. E. Munch, M. E. Launey, D. H. Alsem, E. Saiz, A. P. Tomsia, R. O. Ritchie, Tough, bio-inspired hybrid materials. *Science* **322**, 1516–1520 (2008).
8. A. R. Studart, Bioinspired ceramics: Turning brittleness into toughness. *Nat. Mater.* **13**, 433–435 (2014).
9. F. Bouville, E. Maire, S. Meille, B. Van de Moortèle, A. J. Stevenson, S. Deville, Strong, tough and stiff bioinspired ceramics from brittle constituents. *Nat. Mater.* **13**, 508–514 (2014).
10. U. G. K. Wegst, H. Bai, E. Saiz, A. P. Tomsia, R. O. Ritchie, Bioinspired structural materials. *Nat. Mater.* **14**, 23–36 (2015).
11. F. Bouville, A. R. Studart, Geologically-inspired strong bulk ceramics made with water at room temperature. *Nat. Commun.* **8**, 14655 (2017).
12. Z. Yin, F. Hannard, F. Barthelat, Impact-resistant nacre-like transparent materials. *Science* **364**, 1260–1263 (2019).
13. M. D. Hager, P. Greil, C. Leyens, S. van der Zwaag, U. S. Schubert, Self-healing materials. *Adv. Mater.* **22**, 5424–5430 (2010).
14. S. R. White, N. R. Sottos, P. H. Geubelle, J. S. Moore, M. R. Kessler, S. R. Sriram, E. N. Brown, S. Viswanathan, Autonomic healing of polymer composites. *Nature* **409**, 794–797 (2001).
15. K. S. Toohey, N. R. Sottos, J. A. Lewis, J. S. Moore, S. R. White, Self-healing materials with microvascular networks. *Nat. Mater.* **6**, 581–585 (2007).
16. H. Guo, Y. Han, W. Zhao, J. Yang, L. Zhang, Universally autonomous self-healing elastomer with high stretchability. *Nat. Commun.* **11**, 2037 (2020).
17. K. Van Tittelboom, N. De Belie, Self-healing in cementitious materials—A review. *Materials* **6**, 2182–2217 (2013).
18. N. De Belie, E. Gruyaert, A. Al-Tabbaa, P. Antonaci, C. Baera, D. Bajare, A. Darquennes, R. Davies, L. Ferrara, T. Jefferson, C. Litina, B. Miljevic, A. Otlewska, J. Ranogajec, M. Roig-Flores, K. Paine, P. Lukowski, P. Serna, J.-M. Tulliani, S. Vucetic, J. Wang, H. M. Jonkers, A review of self-healing concrete for damage management of structures. *Adv. Mater. Interfaces* **5**, 1800074 (2018).
19. K. Ando, M.-C. Chu, K. Tsuji, T. Hirasawa, Y. Kobayashi, S. Sato, Crack healing behaviour and high-temperature strength of mullite/SiC composite ceramics. *J. Eur. Ceram. Soc.* **22**, 1313–1319 (2002).
20. K. Ando, K. Furusawa, K. Takahashi, S. Sato, Crack-healing ability of structural ceramics and a new methodology to guarantee the structural integrity using the ability and proof-test. *J. Eur. Ceram. Soc.* **25**, 549–558 (2005).
21. G. M. Song, Y. T. Pei, W. G. Sloof, S. B. Li, J. T. M. De Hosson, S. van der Zwaag, Oxidation-induced crack healing in $Ti_3AlC_2$ ceramics. *Scr. Mater.* **58**, 13–16 (2008).
22. W. G. Sloof, R. Pei, S. A. McDonald, J. L. Fife, L. Shen, L. Boatemaa, A.-S. Farle, K. Yan, X. Zhang, S. van der Zwaag, P. D. Lee, P. J. Withers, Repeated crack healing in MAX-phase ceramics revealed by 4D *in situ* synchrotron x-ray tomographic microscopy. *Sci. Rep.* **6**, 23040 (2016).
23. T. Osada, K. Kamoda, M. Mitome, T. Hara, T. Abe, Y. Tamagawa, W. Nakao, T. Ohmura, A novel design approach for self-crack-healing structural ceramics with 3D networks of healing activator. *Sci. Rep.* **7**, 17853 (2017).
24. N. van Dijk, S. van der Zwaag, Self-healing phenomena in metals. *Adv. Mater. Interfaces* **5**, 1800226 (2018).
25. M. W. Barsoum, M. Radovic, Elastic and mechanical properties of the MAX phases. *Annu. Rev. Mater. Res.* **41**, 195–227 (2011).
26. M. Radovic, M. W. Barsoum, MAX phases: Bridging the gap between metals and ceramics. *Am. Ceram. Soc. Bull.* **92**, 20–27 (2013).
27. M. Sokol, V. Natu, S. Kota, M. W. Barsoum, On the chemical diversity of the MAX phases. *Trends Chem.* **1**, 210–223 (2019).
28. C. J. Gilbert, D. R. Bloyer, M. W. Barsoum, T. El-Raghy, A. P. Tomsia, R. O. Ritchie, Fatigue-crack growth and fracture properties of coarse and fine-grained $Ti_3SiC_2$. *Scr. Mater.* **42**, 761–767 (2000).
29. D. Chen, K. Shirato, M. W. Barsoum, T. El-Raghy, R. O. Ritchie, Cyclic fatigue-crack growth and fracture properties in $Ti_3SiC_2$ ceramics at elevated temperatures. *J. Am. Ceram. Soc.* **84**, 2914–2920 (2001).
30. M. Radovic, M. Barsoum, T. El-Raghy, S. Wiederhorn, Tensile creep of coarse-grained $Ti_3SiC_2$ in the 1000–1200° C temperature range. *J. Alloys Compd.* **361**, 299–312 (2003).
31. R. Bhattacharya, R. Benitez, M. Radovic, N. C. Goulbourne, High strain-rate response and deformation mechanisms in polycrystalline $Ti_2AlC$. *Mater. Sci. Eng. A* **598**, 319–326 (2014).
32. R. Benitez, W. H. Kan, H. Gao, M. O'Neal, G. Proust, A. Srivastava, M. Radovic, Mechanical properties and microstructure evolution of $Ti_2AlC$ under compression in 25-1100 °C temperature range. *Acta Mater.* **189**, 154–165 (2020).
33. G. Plummer, H. Rathod, A. Srivastava, M. Radovic, T. Ouisse, M. Yildizhan, P. O. Å. Persson, K. Lambrinou, M. W. Barsoum, G. J. Tucker, On the origin of kinking in layered crystalline solids. *Mater. Today* **43**, 45–52 (2021).
34. F. Hörz, Static and dynamic origin of kink bands in micas. *J. Geophys. Res.* **75**, 965–977 (1970).
35. M. E. Manley, E. M. Schulson, Kinks and cracks in S1 ice under across-column compression. *Philos. Mag. Lett.* **75**, 83–90 (1997).
36. R. Menig, M. H. Meyers, M. A. Meyers, K. S. Vecchio, Quasi-static and dynamic mechanical response of *Haliotis rufescens* (abalone) shells. *Acta Mater.* **48**, 2383–2398 (2000).
37. M. W. Barsoum, A. Murugaiah, S. R. Kalidindi, T. Zhen, Y. Gogotsi, Kink bands, nonlinear elasticity and nanoindentations in graphite. *Carbon* **42**, 1435–1445 (2004).
38. E. Orowan, A type of plastic deformation new in metals. *Nature* **149**, 643–644 (1942).
39. P. Flewitt, A. Crocker, The formation of deformation kinks in body centred cubic crystals. *Philos. Mag.* **34**, 877–891 (1976).
40. A. G. Evans, W. F. Adler, Kinking as a mode of structural degradation in carbon fiber composites. *Acta Metall.* **26**, 725–738 (1978).
41. B. Budiansky, N. A. Fleck, Compressive failure of fibre composites. *J. Mech. Phys. Solids* **41**, 183–211 (1993).
42. S. Kyriakides, R. Arseculeratne, E. J. Perry, K. M. Liechti, On the compressive failure of fiber reinforced composites. *Int. J. Solids Struct.* **32**, 689–738 (1995).
43. H. Suematsu, T. Suzuki, T. Iseki, T. Mori, Kinking and cracking caused by slip in single crystals of silicon carbide. *J. Am. Ceram. Soc.* **74**, 173–178 (1991).
44. S. Turan, K. M. Knowles, High resolution transmission electron microscopy of the planar defect structure of hexagonal boron nitride. *Phys. Stat. Solidi (a)* **150**, 227–237 (1995).
45. T. Nizolek, N. A. Mara, I. J. Beyerlein, J. T. Avallone, T. M. Pollock, Enhanced plasticity via kinking in cubic metallic nanolaminates. *Adv. Eng. Mater.* **17**, 781–785 (2015).
46. Y. Chen, S. Kota, M. W. Barsoum, M. Radovic, Compressive deformation of MoAlB up to 1100° C. *J. Alloys Compd.* **774**, 1216–1222 (2019).
47. T. Ouisse, E. Sarigiannidou, O. Chaix-Pluchery, H. Roussel, B. Doisneau, D. Chaussende, High temperature solution growth and characterization of $Cr_2AlC$ single crystals. *J. Cryst. Growth* **384**, 88–95 (2013).

48. C. Brüsewitz, I. Knorr, H. Hofsäss, M. W. Barsoum, C. A. Volkert, Single crystal pillar microcompression tests of the MAX phases $Ti_2InC$ and $Ti_4AlN_3$. *Scr. Mater.* **69**, 303–306 (2013).
49. M. Higashi, S. Momono, K. Kishida, N. L. Okamoto, H. Inui, Anisotropic plastic deformation of single crystals of the MAX phase compound $Ti_3SiC_2$ investigated by micropillar compression. *Acta Mater.* **161**, 161–170 (2018).
50. Z. Zhan, Y. Chen, M. Radovic, A. Srivastava, Non-classical crystallographic slip in a ternary carbide—$Ti_2AlC$. *Mater. Res. Lett.* **8**, 275–281 (2020).
51. J. F. Dewey, Nature and origin of kink-bands. *Tectonophysics* **1**, 459–494 (1965).

**Acknowledgments**
**Funding:** The financial support provided by the U.S. National Science Foundation (grants CMMI-1729350 and CMMI-1944496) are gratefully acknowledged. **Author contributions:** H.J.R. built the experimental setup, prepared samples, and carried out all the in situ SEM experiments as well as EBSD and optical microscopy analyses. T.O. synthesized large single crystals of $Cr_2AlC$ used in this study. M.R. and A.S. conceived, planned, and supervised the experimental work. All authors contributed to the analysis of the results and discussion. M.R. and A.S. wrote the manuscript with input from H.J.R. and T.O. All authors have reviewed and approved the manuscript. **Competing interests:** The authors declare that they have no competing interests. **Data and materials availability:** All data needed to evaluate the conclusions in the paper are present in the paper and/or the Supplementary Materials.

Submitted 21 December 2020
Accepted 23 June 2021
Published 11 August 2021
10.1126/sciadv.abg2549

**Citation:** H. J. Rathod, T. Ouisse, M. Radovic, A. Srivastava, Room temperature crack-healing in an atomically layered ternary carbide. *Sci. Adv.* **7**, eabg2549 (2021).

# Room temperature crack-healing in an atomically layered ternary carbide

Hemant J. RathodThierry OuisseMiladin RadovicAnkit Srivastava

*Sci. Adv.*, 7 (33), eabg2549.







*Science Advances* (ISSN ) is published by the American Association for the Advancement of Science. 1200 New York Avenue NW, Washington, DC 20005. The title *Science Advances* is a registered trademark of AAAS.